Ultrahigh Tunneling-Magnetoresistance Ratios in Nitride-Based Perpendicular Magnetic Tunnel Junctions from First Principles

Baishun Yang,[1,2] Lingling Tao,[3] Leina Jiang,[2] Weizhao Chen,[2] Ping Tang,[2] Yu Yan,[1,*] and Xiufeng Han[2,†]

[1]*Key Laboratory of Physics and Technology for Advanced Batteries (Ministry of Education), Department of Physics, Jilin University, Changchun 130012, People's Republic of China*

[2]*Beijing National Laboratory for Condensed Matter Physics, Institute of Physics, University of Chinese Academy of Sciences, Chinese Academy of Sciences, Beijing 100190, China*

[3]*Department of Physics and Astronomy, University of Nebraska, Lincoln, Nebraska 68588, USA*

(Received 13 July 2017; revised manuscript received 12 January 2018; published 14 May 2018)

We report a first-principles study of electronic structures, magnetic properties, and the tunneling-magnetoresistance (TMR) effect of a series of ferromagnetic nitride M_4N (M = Fe, Co, Ni)-based magnetic tunnel junctions (MTJs). It is found that bulk Fe_4N reveals a half-metal nature in terms of the Δ_1 state. A perpendicular magnetic anisotropy is observed in the periodic system Fe_4N/MgO. In particular, the ultrahigh TMR ratio of over 24 000% is predicted in the $Fe_4N/MgO/Fe_4N$ MTJ due to the interface resonance tunneling and relatively high transmission for states of other symmetry. Besides, the large TMR can be maintained with the change of atomic details at the interface, such as the order-disorder interface, the change of thickness of the MgO barrier, and different in-plane lattice constants of the MTJ. The physical origin of the TMR effect can be well understood by analyzing the band structure and transmission channel of bulk Fe_4N as well as the transmission in momentum space of $Fe_4N/MgO/Fe_4N$. Our results suggest that the $Fe_4N/MgO/Fe_4N$ MTJ is a benefit for spintronic applications.

DOI: 10.1103/PhysRevApplied.9.054019

I. INTRODUCTION

The tunneling-magnetoresistance (TMR) effect observed in a magnetic tunnel junction (MTJ) has been extensively studied during the past decades due to its promising application in magnetic read heads and magnetic random access memory [1–7]. A typical MTJ consists of an insulator layer sandwiched by two ferromagnetic layers. The TMR ratio is an important device merit of an MTJ. Tremendous effort has been devoted to obtain a higher TMR ratio. In particular, the high TMR ratio predicted in Fe/MgO/Fe by first-principles calculations has aroused the investigations of MgO-based MTJs [8,9]. Intriguingly, a room-temperature TMR ratio in excess of 600% has been achieved experimentally in a CoFeB/MgO/CoFeB MTJ [10]. Many electrode and barrier materials have been investigated to improve the MTJ device performance, such as Co_2MnSi [11], MnGa [12], and Fe_3Si [13] electrodes as well as spinel oxides [14], $SrTiO_3$ [15], and GaO [16] barriers.

Here, we propose one class of promising electrode materials, namely, ferromagnetic nitrides M_4N (M = Fe, Co, Ni). This choice is motivated by several merits of the materials. First, Fe_4N has low coercivity, high chemical stability, high electrical conductivity, and a high Curie temperature (761 K) [17–20], which are favorable for the application of spin-transfer-torque-based magnetic random access memory [21,22]. Second, it is found that the $Fe_4N/BiFeO_3$ heterostructure [23] possesses a high perpendicular magnetic anisotropy, which is a benefit for high thermal stability, and low critical current density switching in the next-generation high-density nonvolatile memory [24,25]. Third, Fe_4N possesses a perovskite structure which can be epitaxially grown on most oxide substrates such as $SrTiO_3$ and MgO [26–30]. Last, the spin polarization of Fe_4N is as large as 59% (at 7.8 K), as confirmed by point contact Andreev reflection [31]. Experimentally, Sunaga and Tsunoda observe a large TMR ratio of −18.5% under a finite bias in the $Fe_4N/MgO/CoFeB$ MTJ [26]. Furthermore, Komasaki *et al.* observe an even larger TMR ratio of −75.1% under a finite bias in the $Fe_4N/MgO/CoFeB$ MTJ [32]. Also, Tsunoda, Chiba, and Kabara report a TMR ratio of −18.5% in the $Fe_4N/MgAl_2O_4/CoFeB$ MTJ [29]. These works indicate the feasibility of using Fe_4N as the electrodes of MTJs. Moreover, Co_4N and Ni_4N are also synthesized by molecular beam epitaxy and magnetron sputtering techniques [33,34]. On the other hand, the electronic structures and magnetic properties of bulk M_4N (M = Fe, Co, Ni) [19,20,35–40] and the magnetic properties of Fe_4N/oxide (MgO, $BaTiO_3$, and $BiFeO_3$) heterostructures are theoretically investigated from

*yanyu@jlu.edu.cn
†xfhan@iphy.ac.cn

first-principles calculations [39]. However, a theoretical study on the TMR effect and spin-dependent transport in the nitride (M_4N, M = Fe, Co, Ni) -based MTJs is still lacking. It is the purpose of this paper to investigate the TMR effect and magnetic anisotropy in these nitride-based heterostructures by means of first-principles calculations.

II. COMPUTATIONAL METHODOLOGY

First-principles calculations are performed using the projector-augmented-wave method [41] as implemented in the Vienna *ab initio* simulation package [42–44]. An energy cutoff of 500 eV and Perdew-Burke-Ernzerhof [45] generalized-gradient approximation for the exchange-correlation functional are used throughout. Structural relaxations are performed using a $10 \times 10 \times 1k$-point mesh for M_4N/MgO/M_4N (M = Fe, Co, Ni) MTJ until the force on each atom is smaller than 0.01 eV/Å and the total energy converged to less than 1×10^{-5} eV. The magnetic anisotropy energy (MAE) of a periodic system Fe_4N(5 ML)/MgO(5 ML) (ML represents monolayer) is calculated using the force theorem approach [46,47]. The MAE is defined as the energy difference between the magnetic moment aligning in the in-plane and out-of-plane orientations. For the precise calculations of the MAE, a higher-energy convergence of 1×10^{-6} eV and a $15 \times 15 \times 1k$-point mesh are adopted. According to the recipe of the second-order perturbation theory by Wang, Wu, and Freeman [48], the MAE of Fe_4N(5 ML)/MgO(5 ML) can be approximated to the sum of the following two terms:

$$\Delta E^{--} = E^{--}(x) - E^{--}(z) = \xi^2 \sum_{o^-,u^-} \frac{|\langle o^-|L_z|u^-\rangle|^2 - |\langle o^-|L_x|u^-\rangle|^2}{E_u^- - E_o^-}, \quad (1)$$

$$\Delta E^{+-} = E^{+-}(x) - E^{+-}(z) = -\xi^2 \sum_{o^+,u^-} \frac{|\langle o^+|L_z|u^-\rangle|^2 - |\langle o^+|L_x|u^-\rangle|^2}{E_u^- - E_o^+}, \quad (2)$$

where + and − are the majority- and minority-spin states, respectively, and o (u) and E_o (E_u) represent the occupied (unoccupied) eigenstate and corresponding eigenenergy, respectively. The matrix element differences between two different orbitals are listed in our previous paper [47]. Equations (1) and (2) are used to interpret the dominant contributions to the MAE from the partial density of states.

The quantum transport calculations are performed using the Nanodcal package [9], which is based on the state-of-the-art technique by combining the real-space density-functional theory with the Keldysh nonequilibrium Greens function formalism. The spin-polarized conductance G_σ is given by the Landauer-Büttiker formula

$$G_\sigma = \frac{e^2}{h} \sum_{\mathbf{k}_\parallel} T_\sigma(\mathbf{k}_\parallel, E_F), \quad (3)$$

where $T_\sigma(\mathbf{k}_\parallel, E_F)$ is the transmission coefficient at the Fermi level E_F with spin σ ($\sigma = \uparrow, \downarrow$) and transverse Bloch wave vector $k_\parallel = (k_x, k_y)$, e is the electron charge, and h is the Planck constant. A $10 \times 10k_\parallel$ mesh and a $100 \times 100k_\parallel$ mesh are used for self-consistent calculations and evaluating the conductance, respectively. The generalized-gradient approximation as parameterized by Perdew, Burke, and Ernzerhof is used for the exchange-correlation potential [45].

III. RESULTS AND DISCUSSION

A. Structure of bulk M_4N and M_4N/MgO heterostructure

Bulk Fe_4N has a cubic antiperovskite structure, and the experimental lattice constant is 3.795 Å [49], as shown in Fig. 1(a). There are two different "Fe" atoms, in which one locates at the corner (Fe_I) and the other locates at the face center (Fe_{II}). It is clear that the bonding lengths between Fe_I-N and Fe_{II}-N are different, and the electron hybridization between Fe_{II} and N atoms is expected to be more pronounced due to the shorter bond length. To explore the role of the N atom in Fe_4N, we also calculate bulk fcc Fe with the same lattice constant of Fe_4N, which can be simply viewed as taking the N atom away from Fe_4N. It is theoretically reported that the fcc Fe sustains in a stable ferromagnetic phase when the lattice constant is larger than 3.640 Å [50]. The bulk Co_4N and Ni_4N are also calculated as a comparison, and the optimized lattice constant is 3.730 and 3.740 Å, respectively.

The structure of the Fe_4N/MgO heterostructure is also investigated. The in-plane lattice constant is selected as 3.795 Å, which is the same as bulk Fe_4N. The formation energy of the Fe-Fe termination with Fe_I on top of O is −12.526 eV, which is at least 3 times smaller than other termination configurations, including the Fe-Fe termination

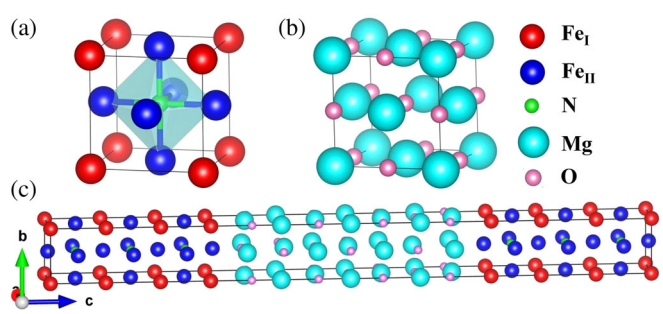

FIG. 1. Atomic structures of (a) Fe_4N and (b) MgO (red, blue, green, light blue, and pink balls represent Fe_I, Fe_{II}, N, Mg, and O atoms, respectively). (c) Optimized atomic structure of the Fe_4N/MgO/Fe_4N MTJ model; the transport direction is along the c axis.

TABLE I. Charge (in units of e) and magnetic moment (in units of μ_B) distribution of bulk fcc Fe and bulk M_4N.

	fcc Fe		Fe_4N			Co_4N			Ni_4N		
Atom	Fe_I	Fe_{II}	Fe_I	Fe_{II}	N	Co_I	Co_{II}	N	Ni_I	Ni_{II}	N
Charge (e)	8.00	8.00	7.80	7.62	6.35	8.79	8.67	6.19	9.85	9.68	6.10
Moment (μ_B)	2.74	2.74	2.94	2.32	0.02	1.92	1.45	0.09	0.71	0.30	0.04
Spin polarization	−47.7%		−54.3%			−82.7%			−52.5%		

with Fe_{II} on top of O, Fe-N termination with Fe_I on top of O, and Fe-N termination with Fe_{II} on top of O. Therefore, the Fe-Fe termination with Fe_I on top of O is preferred with respect to the other three termination configurations, which is the same as the reported result in Ref. [38]. The optimized Fe-O distance at the interface is found to be 1.993 Å. A periodic system Fe_4N(5 ML)/MgO(5 ML) is used to calculate the MAE. The MTJ consists of two semi-infinite Fe_4N electrodes sandwiching seven monolayers of MgO as a barrier shown in Fig. 1 and is used to calculate the magnetic transport property. The lattice mismatch between Co_4N(Ni_4N) and MgO is very large [51–53], and the Co_4N- and Ni_4N-based heterostructures are used for a comparison with the Fe_4N-based heterostructure.

B. Electronic structure and magnetism of bulk M_4N

We first calculate atom-resolved charges, magnetic moments, and spin polarizations of fcc Fe and bulk M_4N (M = Fe, Co, Ni) as reported in Table I. The effective nuclear charges of atoms are obtained from the Bader charge analysis [54]. It is seen that the effective nuclear charge of Fe_I is slightly larger than that of Fe_{II}. This is expected due to the relatively larger hybridization between Fe_{II} and N. The magnetic moment of Fe_I (Fe_{II}) is slightly increased (reduced) in comparison to Fe in fcc Fe. The acquired magnetic moment in N is negligible in all cases. Moreover, the atom-resolved magnetic moment for Fe_4N agrees well with previous results [37]. On the other hand, the spin polarizations for all systems are negative as expected from the 3d-orbital exchange spin splitting. The calculated spin polarization of Fe_4N is −54.3%, which is in consistent with the point-contact Andreev reflection result [31]. The spin polarization for Co_4N is −82.7%, which is larger than that of Fe_4N and Ni_4N.

To understand the above magnetic properties, we plot the partial density of states (PDOS) in Fig. 2. For all systems, the DOS of minority spin is larger than that of majority spin in the vicinity of the Fermi level, which in turn results in the negative spin polarization as listed in Table I. As shown in Fig. 2(b), the occupied states of majority-spin Fe_I-3d states (from −1 to −4 eV) and the unoccupied states of minority-spin Fe_I-3d states (in the range of 0–2 eV) are more than those of Fe_{II}-3d states, which means that the spin splitting of Fe_I-3d is larger than that of Fe_{II}-3d. Correspondingly, the magnetic moment of the Fe_I atom is larger than that of Fe_{II}. The electrons filling in the valence band vary with the 3d element due to the different effective nuclear charges. Since the effective nuclear charge for Co is larger than Fe, the Fermi level for Co_4N is much closer to the DOS peak of minority spin [see Figs. 2(b) and 2(c)]. Thus, the spin polarization for Co_4N is larger than for Fe_4N.

Figure 3 shows the symmetry-resolved band structures of fcc Fe and bulk M_4N (M = Fe, Co, Ni). The band is along the transport direction (Γ-X). For fcc Fe, the majority-spin Δ_1 band crosses the Fermi level, as shown in Fig. 3(a). Thus, fcc Fe reveals a half-metal nature in terms of Δ_1 state along the transport direction, which is similar to bcc Fe [55]. For Fe_4N, the minority Δ_1 and the doubly degenerate Δ_5 bands cross the Fermi level, while no majority bands cross the Fermi level along the transport direction, as shown in Fig. 3(b). This indicates that Fe_4N reveals a half-metal nature in terms of both Δ_1 and Δ_5 states. For bulk Co_4N and Ni_4N, only the minority-spin Δ_5 bands cross the Fermi level, as shown in Figs. 3(c) and 3(d).

C. Magnetic anisotropy energy of M_4N/MgO

The calculated MAE of the periodic system Fe_4N/MgO is 0.856 meV, which is different from the isotropic bulk Fe_4N. The calculated results show that the MAEs of the atoms with the same symmetry are the same. It is noticed that the MAE of all the Fe_I atoms are positive and only the

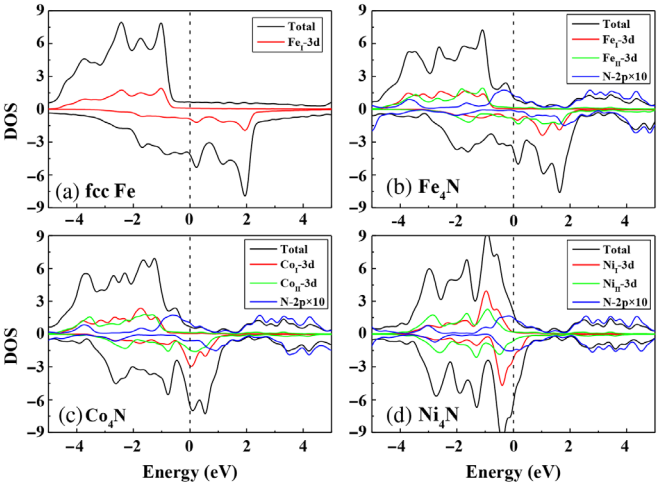

FIG. 2. PDOS of Fe-3d, Co-3d, Ni-3d, and N-2p orbitals and the total DOS of (a) fcc Fe, (b) Fe_4N, (c) Co_4N, and (d) Ni_4N. Note that the PDOS of the N-2p orbital is multiplied by a factor of 10 in order to be shown clearly.

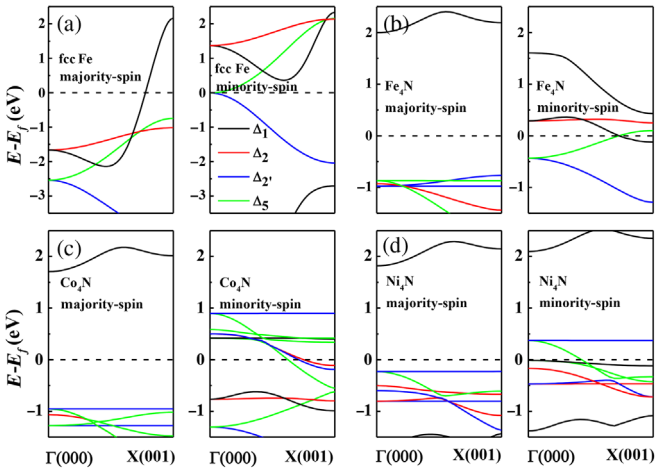

FIG. 3. Symmetry-resolved band structures of (a) fcc Fe, (b) Fe_4N, (c) Co_4N, and (d) Ni_4N, respectively. The Fermi level E_F is set to zero.

interface Fe_{II} atoms possess a positive MAE. As shown in Fig. 4(a), the interface Fe_I and Fe_{II} atoms (labeled as Fe_I-1 and Fe_{II}-1) provide the largest contribution to the positive MAE, while the middle layer Fe_{II} atoms (Fe_{II}-3) provide a negative contribution to the MAE. Therefore, the perpendicular magnetic anisotropy of Fe_4N/MgO is an interfacial effect. It is interesting that not only do Fe_I and Fe_{II} provide different contributions to the MAE, but also the MAE of Fe_{II} in different layers are also different. The different MAEs of these atoms are discussed in the following.

Figure 4(b) depicts the orbital-resolved MAE of the three representative Fe atoms, such as Fe_I-1, Fe_{II}-1, and Fe_{II}-2. For Fe_I-1, the matrix element difference between d_{yz} and d_{z^2} shows the largest positive value, and the matrix element difference between d_{yz} and d_{xz} also has a large contribution, which results in the out-of-plane easy magnetic axis in Fe_I-1. For Fe_{II}-1, the matrix element difference between d_{xy} and $d_{x^2-y^2}$ provides the largest positive contribution to the MAE, while the matrix element difference between d_{yz} and d_{z^2} provides only a small positive contribution to the MAE. For Fe_{II}-2, the positive contributions from the matrix element difference between d_{xy} and $d_{x^2-y^2}$ are small, and the matrix element difference between d_{yz} and d_{z^2} shows a large negative value, which results in the in-plane easy magnetic axis in Fe_{II}-2. To further shed light on the origin of the different contributions to the MAE from different Fe atoms, we combine the density of states and Eqs. (1) and (2) to analyze the mechanism.

It can be concluded from Eqs. (1) and (2) that the occupied and unoccupied orbitals in the vicinity of the Fermi level contribute the most to the MAE. Among the occupied and unoccupied orbitals in the vicinity of the Fermi level, the energy differences between d_{yz}^{u-} and $d_{z^2}^{o+}$ of Fe_I-1 [ΔE_1 in Fig. 4(c)] and $d_{x^2-y^2}^{u-}$ and d_{xy}^{o-} of Fe_{II}-1 [ΔE_2 in Fig. 4(c)], as well as d_{yz}^{u-} and $d_{z^2}^{o-}$ of Fe_{II}-2 [ΔE_3 in Fig. 4(c)] are small, which means that they contribute the most to the MAE of the three different Fe atoms. It is known that the matrix element differences to the MAE

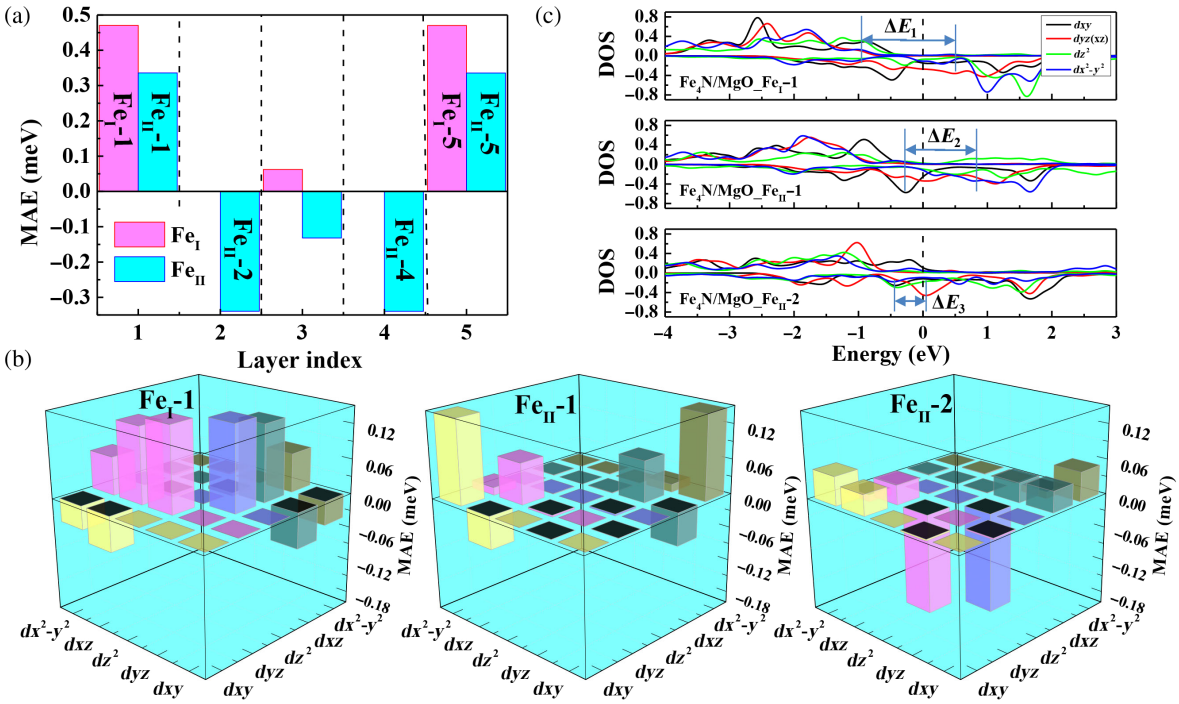

FIG. 4. (a) Atom-resolved MAE of periodic system Fe_4N(5 ML)/MgO; atoms in different layers are labeled with the number. (b) d-orbital-resolved MAE of the selective Fe_I-1, Fe_{II}-1, and Fe_{II}-2 atoms. (c) DOS of the d orbitals of the above three atoms.

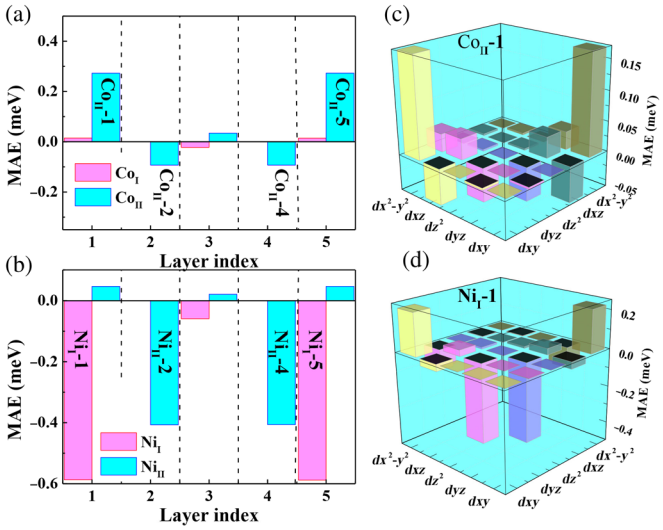

FIG. 5. Atom-resolved MAE of (a) Co_4N(5 ML)/MgO(5 ML) and (b) Ni_4N(5 ML)/MgO(5 ML) and d-orbital-resolved MAE of a (c) Co_I-1 and (d) Ni_I-1 atom.

between the same spins are opposite to that of opposite spins [47]. Therefore, the matrix element difference between d_{yz} and d_{z^2} shows a positive contribution to the MAE of Fe_I-1 and a negative contribution to the MAE of Fe_{II}-2, respectively. For other matrix element differences between two occupied and unoccupied orbitals of Fe, atoms can also be well discussed from Eqs. (1) and (2) and the corresponding density of states.

Furthermore, we calculate the magnetic anisotropy energy of the periodic system Co_4N(5 ML)/MgO(5 ML) and Ni_4N(5 ML)/MgO(5 ML). The calculated MAEs of Co_4N/MgO and Ni_4N/MgO heterostructures are 0.390 and −2.052 meV, respectively. Combining the atom- and orbital-resolved MAE calculations, we find that the positive and negative MAEs of the two periodic systems mainly come from the d_{xy} and $d_{x^2-y^2}$ orbitals of the Co_{II}-1 atom and the d_{yz} and d_{z^2} orbitals of the Ni_I-1 atom, as shown in Fig. 5. Therefore, the out-of-plane easy axis of Co_4N/MgO and in-plane easy axis of Ni_4N/MgO are also an interfacial effect.

D. TMR effect and spin-dependent transport

The MTJ model used for performing quantum transport calculations for the MTJs is shown in Fig. 1(c). The TMR ratio is defined as $\mathrm{TMR} = (G_{\mathrm{PC}} - G_{\mathrm{APC}})/G_{\mathrm{APC}}$, where G_{PC} and G_{APC} are the total conductance for the magnetizations of two electrodes in parallel (PC) and antiparallel (APC) configurations, respectively. The spin-dependent $G^{\uparrow}_{\mathrm{PC}}$, $G^{\downarrow}_{\mathrm{PC}}$, $G^{\uparrow}_{\mathrm{APC}}$, and $G^{\downarrow}_{\mathrm{APC}}$ as well as the TMR for four MTJs are listed in Table II. For fcc Fe/MgO/fcc Fe, $G^{\uparrow}_{\mathrm{PC}}$ is larger than $G^{\downarrow}_{\mathrm{PC}}$ due to the slow decay of the majority-spin Δ_1 state through the MgO barrier, as confirmed from the band structure [see Fig. 3(a)]. Furthermore, $G^{\uparrow}_{\mathrm{APC}}$ and $G^{\downarrow}_{\mathrm{APC}}$ are significantly reduced due to the half-metallicity of the Δ_1 state, and a TMR ratio of more than 1000% is observed due to the Δ_1 spin spin-filtering effect. The spin-dependent transport property of fcc Fe/MgO/fcc Fe MTJ is similar to that of the bcc Fe/MgO/bcc Fe MTJ [8]. In the case of Fe_4N/MgO/Fe_4N, $G^{\uparrow}_{\mathrm{PC}}$ is smaller than $G^{\downarrow}_{\mathrm{PC}}$ and the conductance in PC is about 2 orders of magnitude larger than that in APC. Consequently, an ultrahigh TMR ratio of more than 20000% is obtained in Fe_4N/MgO/Fe_4N, which is significantly larger than that of fcc Fe/MgO/fcc Fe.

For a comprehensive understanding of the above spin-dependent conductance and TMR effect, we plot the distribution of transmission coefficients in the two-dimensional Brillouin zone (BZ), as shown in Fig. 6. For fcc Fe/MgO/fcc Fe, the majority spin in PC shows broad peaks around the center of the BZ due to the slow decay from the Δ_1 state [Fig. 6(a)], while the minority-spin transmission in PC is characterized by sharp peaks [Fig. 6(b)] at some special $k_{\parallel}$ points, which come from the interface resonant transmission. As evident from the band structure shown in Fig. 3(b), there are no incoming majority-spin Δ_1 states at the Fermi level for Fe_4N. Therefore, for the Fe_4N/MgO/Fe_4N MTJ, the majority-spin transmission in PC is negligible around the center of the BZ. In contrast, the minority-spin tunneling shows large peaks around the center of the two-dimensional Brillouin zone. Note that, although the transmission around the center of the BZ is negligible for a minority spin in PC, the transmission originating from the contribution of interface resonant states is very large. Besides, there are also several areas regularly distributed in the BZ that reveal a relatively high transmission for states of other symmetries [green and yellow parts in Fig. 6(e)].

TABLE II. Spin-dependent conductance G_σ (in units of e^2/h) and TMR ratios (in percent) for a series of MTJs. $G^{\uparrow}_{\mathrm{PC}}$ and $G^{\downarrow}_{\mathrm{PC}}$ are the majority-spin and minority-spin conductance in PC, respectively. $G^{\uparrow}_{\mathrm{APC}}$ and $G^{\downarrow}_{\mathrm{APC}}$ are the majority-spin and minority-spin conductance in APC, respectively. The majority spin and minority spin refer to the left electrode.

Structure	$G^{\uparrow}_{\mathrm{PC}}$	$G^{\downarrow}_{\mathrm{PC}}$	$G^{\uparrow}_{\mathrm{APC}}$	$G^{\downarrow}_{\mathrm{APC}}$	TMR (%)
fcc Fe/MgO/fcc Fe	2.01×10^{-5}	0.09×10^{-5}	9.49×10^{-7}	9.33×10^{-7}	1014
Fe_4N/MgO/Fe_4N	0.81×10^{-5}	5.47×10^{-5}	1.26×10^{-7}	1.28×10^{-7}	24 711
Co_4N/MgO/Co_4N	0.14×10^{-5}	2.49×10^{-5}	1.40×10^{-6}	0.53×10^{-6}	1269
Ni_4N/MgO/Ni_4N	0.89×10^{-5}	1.53×10^{-5}	7.18×10^{-7}	7.79×10^{-7}	1514

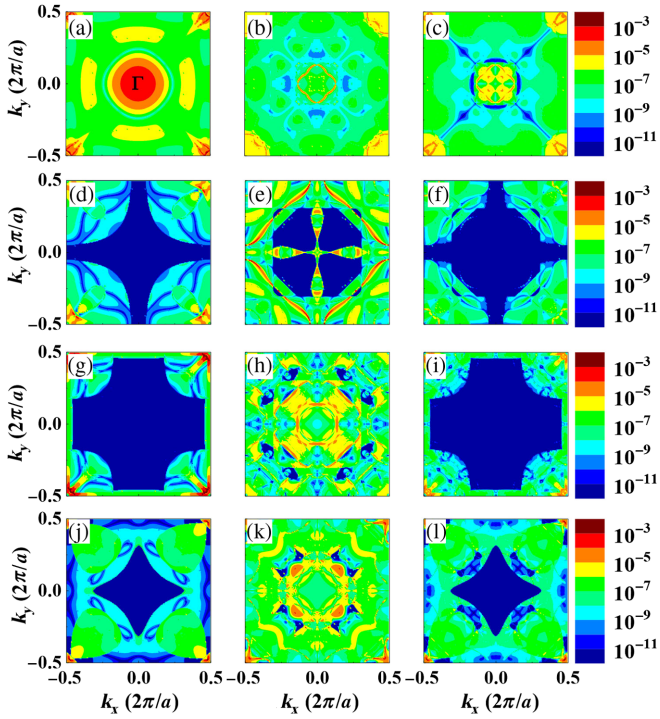

FIG. 6. The $k_{\parallel}$-resolved transmission coefficients of (a)–(c) fcc Fe/MgO/fcc Fe, (d)–(f) Fe_4N/MgO/Fe_4N, (g)–(i) Co_4N/MgO/Co_4N, and (j)–(l) Ni_4N/MgO/Ni_4N MTJs under zero bias. (a), (d), (g), and (j) show majority to majority in PC. (b), (e), (h), and (k) show minority to minority in PC. (c), (f), (i), and (l) show majority to minority or minority to majority in APC.

The calculated TMR ratio of Co_4N/MgO/Co_4N and Ni_4N/MgO/Ni_4N MTJs is 1269% and 1514%, respectively, which is much smaller than that of the Fe_4N/MgO/Fe_4N MTJ. As listed in Table II, the conductance in an antiparallel channel of Co_4N- and Ni_4N-based MTJs is much higher than that of the Fe_4N/MgO/Fe_4N MTJ, which may be the reason why the TMR of the Co_4N- and Ni_4N-based MTJs is much smaller than that of the Fe_4N/MgO/Fe_4N MTJ. As is known, the lattice mismatch between Co_4N(Ni_4N) and MgO is very large, that would prevent real experimental heterostructure growth [51–53]. It is supposed that the insertion of a buffer layer in the middle of Co_4N(Ni_4N) and MgO may be a good strategy to synthesize the stable Co_4N- and Ni_4N-based MgO barrier heterostructure. As mentioned above, the anisotropy of the Co_4N/MgO and Ni_4N/MgO systems is not always perpendicular. Therefore, only the Fe_4N/MgO/Fe_4N MTJ is fully discussed in this paper.

It is known that the interface resonant state is very sensitive to the atomic details of the interface [56]. Therefore, we calculate the transport properties and TMR of Fe_4N/MgO/Fe_4N MTJs with various interface conditions, including disorder at the interface, different barrier thicknesses, and several in-plane lattice constants. First, in order to investigate the effect of disorder at the interface on the TMR of MTJs, we calculate the magnetic transport property of the nonrelaxed Fe_4N/MgO(7 ML)/Fe_4N MTJ, which corresponds to an interface-ordered MTJ. The results show that, though the calculated TMR ratio for the interface-ordered MTJ decreases compared to a disordered MTJ (24 711%), it is still as high as 10 100%. Then, in order to investigate the influence of the barrier thickness on the TMR, the thickness of the MgO barrier of a nonrelaxed MTJ is set as 5 and 9 ML, besides the above-mentioned 7 ML. For the nonrelaxed Fe_4N/MgO(5 ML)/Fe_4N and Fe_4N/MgO(9 ML)/Fe_4N MTJs, the calculated TMR ratio is as high as 13 027% and 8140%, respectively. Results indicate that, for nonrelaxed Fe_4N/MgO(5 ML)/Fe_4N, Fe_4N/MgO(7 ML)/Fe_4N, and Fe_4N/MgO(9 ML)/Fe_4N MTJs, the conductance for a minority channel in the parallel configuration is still very high compared with the conductance of the other three channels. Therefore, for the interface-disordered or -ordered Fe_4N/MgO/Fe_4N MTJ and Fe_4N/MgO/Fe_4N with different barrier thicknesses, the TMR can maintain a high value. Last, three different in-plane lattice constants for a nonrelaxed Fe_4N/MgO(7 ML)/Fe_4N MTJ are used in our calculations to investigate the influence of in-plane lattice constants on the TMR. The three in-plane lattice constants are selected as 3.795 Å (the lattice constant of Fe_4N), 4.211 Å (lattice constant of MgO), and 4.000 Å (average lattice constant of Fe_4N and MgO). In this part, first of all with the fixed in-plane lattice constants we optimize the out-plane lattice constants of Fe_4N and MgO, and then we optimize the interface distance between Fe_4N and MgO. Figure 7 displays the $k_{\parallel}$-resolved transmission coefficients for MTJs with three different in-plane lattice constants. It can be seen that the dominant contribution to the high conductance comes from the PC-down channel. In order to clarify the high conductance of the PC-down channel for the Fe_4N/MgO/Fe_4N system, we separate the contributions from Delta-symmetry filtering, resonant states (red parts), and other states of other symmetries (green and yellow parts) in Fig. 6(e). It is found that the contributions to the conductance in the PC-down channel from other states of other symmetries are as high as 59.74%. Therefore, the high conductance in Fig. 6(e) comes not only from the resonant states, but also other states of other symmetries provide large contributions. Similarly, other states of other symmetries also play an important role for the conductance in the PC-down channel of ordered Fe_4N/MgO/Fe_4N MTJs with different in-plane lattice constants, as shown in Figs. 7(b), 7(e), and 7(h). Besides, it can be seen from the transmission around the Gamma point in Figs. 7(e) and 7(h) that the Δ_1-symmetry tunneling transmission occurs when the in-plane lattice constants increase to 4.000 and 4.211 Å.

As is known, the transmission coefficient of Fe_4N/MgO/Fe_4N in the BZ should be related to the transmission channel of bulk Fe_4N. Therefore, to shed light on the above issues, we calculate the transmission minority channel of

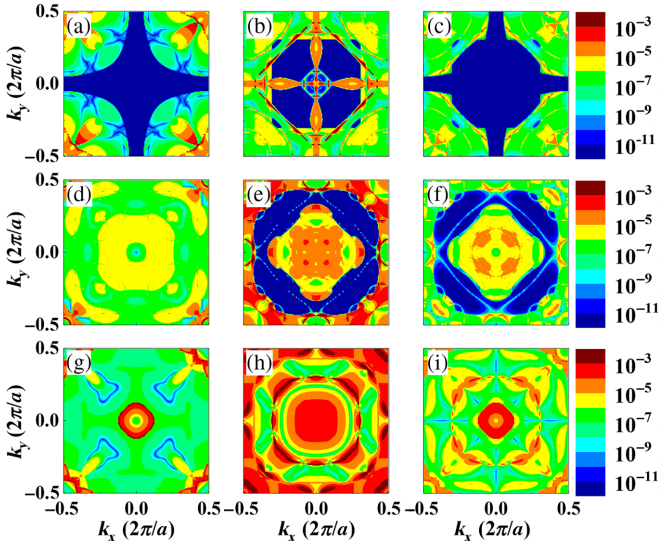

FIG. 7. The $k_{\parallel}$-resolved transmission coefficients of an ordered $Fe_4N/MgO/Fe_4N$ MTJ with different in-plane lattice constants (a)–(c) $a = 3.795$ Å, (d)–(f) $a = 4.000$ Å, and (g)–(i) $a = 4.211$ Å. (a), (d), and (g) show majority to majority in PC. (b), (e), and (h) show minority to minority in PC. (c), (f), and (i) show majority to minority or minority to majority in APC.

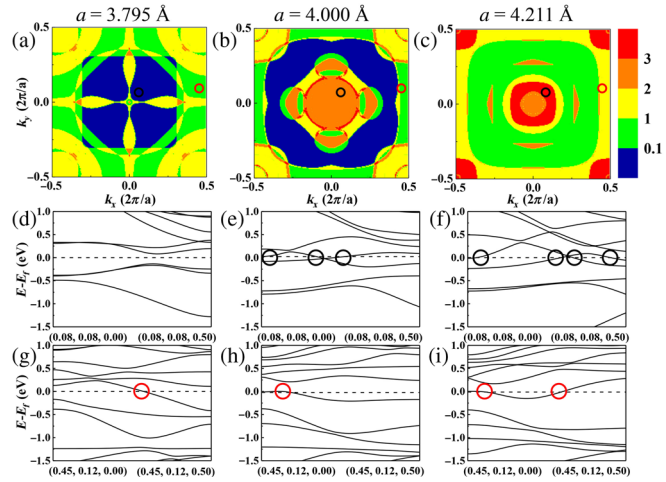

FIG. 8. Transmission minority channel of bulk Fe_4N with in-plane lattice constants of (a) 3.795, (b) 4.000, and (c) 4.211 Å. The minority band structure of bulk Fe_4N (d)–(f) from (0.08, 0.08, 0.00) to (0.08, 0.08, 0.50) and (g)–(i) from (0.45, 0.12, 0.00) to (0.45, 0.12, 0.50) with different in-plane lattice constants.

bulk Fe_4N with different lattice constants as a function of $k_{\parallel}$ at the Fermi level and the corresponding minority band structure, as shown in Fig. 8. It is clear that the regularly distributed areas (green and yellow parts) in Fig. 7(b) correspond to the transmission channels of e^2/h (green parts) and $2e^2/h$ (yellow parts) in Fig. 8(a). Similarly, the areas regularly distributed in Figs. 6(e), 7(e), and 7(h) also correspond to the transmission channel of bulk Fe_4N in Figs. 8(a)–8(c). As shown in Figs. 7(b), 7(e), and 7(h), these regular areas also provide a non-negligible contribution to the conductance of ordered $Fe_4N/MgO/Fe_4N$ with different lattice constants. Furthermore, Figs. 8(a)–8(c) show that the transmission channel of bulk Fe_4N with different in-plane lattice constants is in range 0–4. Meanwhile, with the in-plane lattice constant increases, the transmission channel at the same k point also changes. For example, the transmission channel at ($k_x = 0.08$, $k_y = 0.08$) [in the unit of $2\pi/a$, black circle in Figs. 8(a)–8(c)] of Fe_4N with an in-plane lattice of 3.795, 4.000, and 4.211 Å is 0, 3, and 4, respectively (in the unit of e^2/h), and the transmission channel at ($k_x = 0.45$, $k_y = 0.12$) [red circle in Figs. 8(a)–8(c)] is 1, 1, and 2, respectively. Figures 8(d)–8(f) show the minority band structure of bulk Fe_4N from (0.08, 0.08, 0) to (0.08, 0.08, 0.5) for in-plane lattice constants of 3.795, 4.000, and 4.211 Å. As shown in Figs. 8(d)–8(f), when the in-plane lattice constant of bulk Fe_4N is equal to 3.795, 4.000, and 4.211 Å, branches of the band which cross the Fermi level are 0, 3, and 4, respectively, which induces the change of the transmission channel at ($k_x = 0.08$, $k_y = 0.08$) from 0 to 3 and 4 [57]. Similarly, the change of the transmission channel at ($k_x = 0.45$, $k_y = 0.12$) can also be explained by the minority band structure in Figs. 8(g)–8(i).

For the practical application of a MTJ-based device, the output voltage V_{out} is another important parameter. V_{out} is defined as $V_{\text{out}} = V_b(G_{\text{PC}} - G_{\text{APC}})/G_{\text{PC}}$, where V_b is the applied bias. The bias dependence of the TMR and V_{out} can be obtained through the spin-dependent current I_σ, which is given by the Landauer formula

$$I_\sigma = \frac{e}{h}\int_{\mu_l}^{\mu_r} T_\sigma(E,V)[f_l(E-\mu_l) - f_r(E-\mu_r)]dE, \quad (4)$$

where e is the electron charge, h is the Planck constant, f_l (f_r) is the Fermi distribution function of the left (right) electrode, μ_l (μ_r) is the electrochemical potential of the left (right) electrode, and $\mu_l - \mu_r = eV_b$. The TMR ratio under a finite bias is defined as TMR $= (I_{\text{PC}} - I_{\text{APC}})/I_{\text{APC}}$, with I_{PC} (I_{APC}) being the total current for a MTJ in PC (APC). Figure 9 shows the bias dependence of the TMR ratios of $Fe_4N/MgO/Fe_4N$ and fcc Fe/MgO/fcc Fe MTJs. For $Fe_4N/MgO/Fe_4N$, the TMR decreases monotonically with the bias and the TMR is still close to 2000% under the bias of 11 mV. In the case of the fcc Fe/MgO/fcc Fe MTJ, though the TMR oscillates with the bias slightly, it still maintains up to a larger bias. For example, the TMR is still over 800% under the bias of 11 mV. Moreover, V_{out} monotonically increases with the increase of V_b for both of the MTJs. Because of the larger TMR ratio for $Fe_4N/MgO/Fe_4N$, the V_{out} of $Fe_4N/MgO/Fe_4N$ is larger than that of fcc Fe/MgO/fcc Fe.

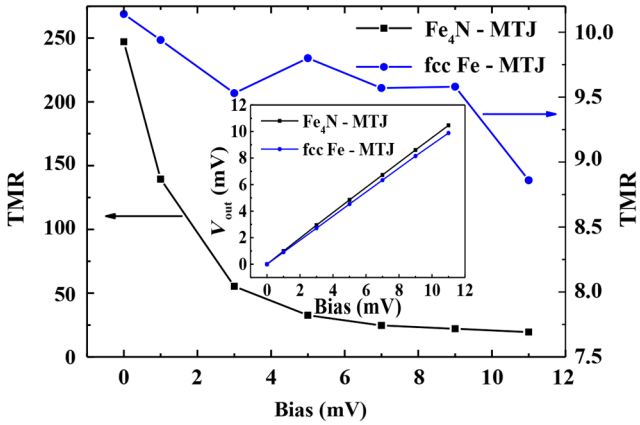

FIG. 9. Bias-dependent TMR ratio of $Fe_4N/MgO/Fe_4N$ (black curve) and fcc Fe/MgO/fcc Fe MTJs (blue curve). The inset indicates a bias-dependent output voltage of $Fe_4N/MgO/Fe_4N$ (black curve) and fcc Fe/MgO/fcc Fe MTJs (blue curve).

IV. CONCLUSION

In summary, we investigate the electronic structures and magnetic properties of M_4N (M = Fe, Co, Ni), the MAE of the M_4N/MgO heterostructure, and the spin-dependent transport properties of $M_4N/MgO/M_4N$ (M = Fe, Co, Ni) MTJs by means of first-principles calculations. The effective nuclear charges and magnetic moments in bulk Fe_4N are slightly different from those in bulk fcc Fe. Bulk fcc Fe reveals a half-metal nature in terms of the majority-spin Δ_1 state, while bulk Fe_4N reveals a half-metal nature in term of minority-spin Δ_1 and Δ_5 states. Interestingly, the perpendicular magnetic anisotropy is observed in the periodic system Fe_4N/MgO. More importantly, the ultrahigh TMR ratio of over 24 000% is predicted in a relaxed $Fe_4N/MgO/Fe_4N$ MTJ under zero bias due to interface resonance states and a relatively high transmission for states of other symmetries. Furthermore, the large TMR ratio can be maintained with the change of atomic details at the interface, such as the order-disorder interface, the change of thickness of the MgO barrier, and different in-plane lattice constants of the MTJ. Moreover, the TMR of the $Fe_4N/MgO/Fe_4N$ MTJ can maintain up to nearly 2000% in the bias of 11 mV. Our results provide some fundamental understanding of spin-dependent transport through nitride-based perpendicular magnetic tunnel junctions and suggest that a perpendicular $Fe_4N/MgO/Fe_4N$ MTJ can possess a large TMR effect, which is useful for the design of MTJ-based spintronic devices.

ACKNOWLEDGMENTS

This work is supported by the 863 Plan Project of Ministry of Science and Technology (MOST, No. 2014AA032904), the MOST National Key Scientific Instrument and Equipment Development Projects [Grant No. 2011YQ120053], the National Natural Science Foundation of China (NSFC, Grants No. 11434014, No. 51229101, and No. 51620105004), the Strategic Priority Research Program (B) of the Chinese Academy of Sciences (CAS, Grant No. XDB07030200), and the user fund of Wuhan National High Magnetic Field Center (PHMFF2015011). The work is carried out at National Supercomputer Center in Tianjin, and the calculations are performed on TianHe-1 (A). We are also grateful for the support provided by National Natural Science Foundation of China (11174104) and Special Program for Applied Research on Super Computation of the NSFC-Guangdong Joint Fund (the second phase) under Grant No. U1501501.

[1] T. Miyazaki and N. Tezuka, Giant magnetic tunneling effect in $Fe/Al_2O_3/Fe$ junction, J. Magn. Magn. Mater. **139**, L231 (1995).

[2] J. S. Moodera, Lisa R. Kinder, Terrilyn M. Wong, and R. Meservey, Large Magnetoresistance at Room Temperature in Ferromagnetic Thin Film Tunnel Junctions, Phys. Rev. Lett. **74**, 3273 (1995).

[3] X. F. Han, M. Oogane, H. Kubota, Y. Ando, and T. Miyazaki, Fabrication of high-magnetoresistance tunnel junctions using $Co_{75}Fe_{25}$ ferromagnetic electrodes, Appl. Phys. Lett. **77**, 283 (2000).

[4] D. Wang, C. Nordman, J. M. Daughton, Z. Qian, and J. Fink, 70% TMR at room temperature for SDT sandwich junctions with CoFeB as free and reference layers, IEEE Trans. Magn. **40**, 2269 (2004).

[5] S. S. P. Parkin, C. Kaiser, A. Panchula, P. M. Rice, B. Hughes, M. Samant, and S. Yang, Giant tunnelling magnetoresistance at room temperature with MgO (100) tunnel barriers, Nat. Mater. **3**, 862 (2004).

[6] S. Yuasa, T. Nagahama, A. Fukushima, Y. Suzuki, and Koji Ando, Giant room-temperature magnetoresistance in single-crystal Fe/MgO/Fe magnetic tunnel junctions, Nat. Mater. **3**, 868 (2004).

[7] S. Ikeda, J. Hayakawa, Y. M. Lee, F. Matsukura, Y. Ohno, T. Hanyu, and H. Ohno, Magnetic tunnel junctions for spintronic memories and beyond, IEEE Trans. Electron Devices **54**, 991 (2007).

[8] W. H. Butler, X.-G. Zhang, T. C. Schulthess, and J. M. MacLaren, Spin-dependent tunneling conductance of Fe|MgO|Fe sandwiches, Phys. Rev. B **63**, 054416 (2001).

[9] J. Taylor, H. Guo, and J. Wang, *Ab initio* modeling of quantum transport properties of molecular electronic devices, Phys. Rev. B **63**, 245407 (2001).

[10] S. Ikeda, J. Hayakawa, Y. Ashizawa, Y. Lee, K. Miura, H. Hasegawa, M. Tsunoda, F. Matsukura, and H. Ohno, Tunnel magnetoresistance of 604% at 300 K by suppression of Ta diffusion in CoFeB/MgO/CoFeB pseudo-spin-valves annealed at high temperature, Appl. Phys. Lett. **93**, 082508 (2008).

[11] Y. Miura, H. Uchida, Y. Oba, K. Abe, and M. Shirai, Half-metallic interface and coherent tunneling in $Co_2YZ/MgO/Co_2YZ$ (Y, Z = MnSi, CrAl) magnetic tunnel junctions: A first-principles study, Phys. Rev. B **78**, 064416 (2008).

[12] Z. Bai, Y. Cai, L. Shen, M. Yang, V. Ko, G. Han, and Y. Feng, Magnetic and transport properties of

$Mn_{3-x}Ga/MgO/Mn_{3-x}Ga$ magnetic tunnel junctions: A first-principles study, Appl. Phys. Lett. **100**, 022408 (2012).

[13] L. L. Tao, S. H. Liang, D. P. Liu, H. X. Wei, Jian Wang, and X. F. Han, Tunneling magnetoresistance in $Fe_3Si/MgO/Fe_3Si$ (001) magnetic tunnel junctions, Appl. Phys. Lett. **104**, 172406 (2014).

[14] J. Zhang, X.-G. Zhang, and X. F. Han, Spinel oxides: Δ_1 spin-filter barrier for a class of magnetic tunnel junctions, Appl. Phys. Lett. **100**, 222401 (2012).

[15] J. P. Velev, K. D. Belashchenko, D. A. Stewart, M. van Schilfgaarde, S. S. Jaswal, and E. Y. Tsymbal, Negative Spin Polarization and Large Tunneling Magnetoresistance in Epitaxial $Co|SrTiO_3|Co$ Magnetic Tunnel Junctions, Phys. Rev. Lett. **95**, 216601 (2005).

[16] N. Matsuo, N. Doko, T. Takada, H. Saito, and S. Yuasa, High Magnetoresistance in Fully Epitaxial Magnetic Tunnel Junctions with a Semiconducting GaO_x Tunnel Barrier, Phys. Rev. Applied **6**, 034011 (2016).

[17] B. Yu, L. Lin, B. Ma, Z. Z. Zhang, Q. Y. Jin, and J. P. Wang, Fabrication and physical properties of $[Fe/Fe_4N]$ N multilayers with high saturation magnetization, AIP Adv. **6**, 056108 (2016).

[18] S. Kokado, N. Fujima, K. Harigaya, H. Shimizu, and A. Sakuma, Theoretical analysis of highly spin-polarized transport in the iron nitride Fe_4N, Phys. Rev. B **73**, 172410 (2006).

[19] N. Feng, W. B. Mi, Y. C. Cheng, Z. B. Guo, U. Schwingenschlögl, and H. L. Bai, Magnetism by interfacial hybridization and p-type doping of MoS_2 in Fe_4N/MoS_2 superlattices: A first-principles study, ACS Appl. Mater. Interfaces **6**, 4587 (2014).

[20] Q. Zhang, W. B. Mi, X. C. Wang, and X. H. Wang, Spin polarization inversion at benzene-absorbed Fe_4N surface, Sci. Rep. **5**, 10602 (2015).

[21] F. Albert, P. Nguyen, M. Pakala, and T. Valet, Observation of spin-transfer switching in deep submicron-sized and low-resistance magnetic tunnel junctions, Appl. Phys. Lett. **84**, 3118 (2004).

[22] Z. T. Diao, D. Apalkov, M. Pakala, Y. F. Ding, A. Panchula, and Y. M. Huai, Spin transfer switching and spin polarization in magnetic tunnel junctions with MgO and AlO_x barriers, Appl. Phys. Lett. **87**, 232502 (2005).

[23] L. Yin, W. B. Mi, and X. C. Wang, Perpendicular Magnetic Anisotropy and High Spin Polarization in Tetragonal $Fe_4N/BiFeO_3$ Heterostructures, Phys. Rev. Applied **6**, 064022 (2016).

[24] S. Ikeda, K. Miura, H. Yamamoto, K. Mizunuma, H. D. Gan, M. Endo, S. Kanai, J. Hayakawa, F. Matsukura, and H. Ohno, A perpendicular-anisotropy CoFeB-MgO magnetic tunnel junction, Nat. Mater. **9**, 721 (2010).

[25] H. X. Yang, M. Chshiev, B. Dieny, J. H. Lee, A. Manchon, and K. H. Shin, First-principles investigation of the very large perpendicular magnetic anisotropy at Fe|MgO and Co|MgO interfaces, Phys. Rev. B **84**, 054401 (2011).

[26] K. Sunaga and M. Tsunoda, Inverse tunnel magnetoresistance in magnetic tunnel junctions with an Fe_4N electrode, J. Appl. Phys. **102**, 013917 (2007).

[27] S. Atiq, H.-S. Ko, S. A. Siddiqi, and S.-C. Shin, Effect of epitaxy and lattice mismatch on saturation magnetization of γ-Fe_4N thin films, Appl. Phys. Lett. **92**, 222507 (2008).

[28] M. Tsunoda, Y. Komasaki, S. Kokado, S. Isogami, C.-C. Chen, and M. Takahashi, Negative anisotropic magnetoresistance in Fe_4N Film, Appl. Phys. Express **2**, 083001 (2009).

[29] M. Tsunoda, R. Chiba, and K. Kabara, Fabrication of $MgAl_2O_4$ tunnel barrier by radio frequency-sputtering method and magnetoresistance effect through it with Fe or Fe_4N ferromagnetic electrode, J. Appl. Phys. **117**, 17D703 (2015).

[30] Y. Takahashi, T. Miyamachi, S. Nakashima, N. Kawamura, Y. Takagi, M. Uozumi, V. N. Antonov, T. Yokoyama, A. Ernst, and F. Komori, Thickness-dependent electronic and magnetic properties of γ-Fe_4N atomic layers on Cu (001), Phys. Rev. B **95**, 224417 (2017).

[31] A. Narahara, K. Ito, T. Suemasu, Y. K. Takahashi, A. Ranajikanth, and K. Hono, Spin polarization of Fe_4N thin films determined by point-contact Andreev reflection, Appl. Phys. Lett. **94**, 202502 (2009).

[32] Y. Komasaki, M. Tsunoda, S. Isogami, and M. Takahashi, 75% inverse magnetoresistance at room temperature in $Fe_4N/MgO/CoFeB$ magnetic tunnel junctions fabricated on Cu underlayer, J. Appl. Phys. **105**, 07C928 (2009).

[33] K. Ito, T. Sanai, Y. Yasutomi, S. Zhu, K. Toko, Y. Takeda, Y. Saitoh, A. Kimura, and T. Suemasu, X-ray magnetic circular dichroism for $Co_xFe_{4-x}N$ ($x = 0$, 3, 4) films grown by molecular beam epitaxy, J. Appl. Phys. **115**, 17C712 (2014).

[34] A. Linnik, A. Prudnikov, R. Shalaev, T. Linnik, V. Varyukhin, S. Kostyrya, and V. Burkhovetskii, Magnetic properties and thermal modification of nanostructured films of nickel nitrides, Tech. Phys. Lett. **39**, 143 (2013).

[35] Y. Takahashi, Y. Imai, and T. Kumagai, Spin-polarized electronic band structures of the Fe_4N-Co_4N system, J. Magn. Magn. Mater. **323**, 2941 (2011).

[36] S. F. Matar, A. Houari, and M. A. Belkhir, *Ab initio* studies of magnetic properties of cobalt and tetracobalt nitride Co_4N, Phys. Rev. B **75**, 245109 (2007).

[37] P. Monachesi, T. Björkman, T. Gasche, and O. Eriksson, Electronic structure and magnetic properties of Mn, Co, and Ni substitution of Fe in Fe_4N, Phys. Rev. B **88**, 054420 (2013).

[38] P. Hemzalová, M. Friák, M. Šob, D. Ma, A. Udyansky, D. Raabe, and J. Neugebauer, *Ab initio* study of thermodynamic, electronic, magnetic, structural, and elastic properties of Ni_4N allotropes, Phys. Rev. B **88**, 174103 (2013).

[39] N. Feng, W. B. Mi, X. C. Wang, and H. L. Bai, The magnetism of Fe_4N/oxides (MgO, $BaTiO_3$, $BiFeO_3$) interfaces from first-principles calculations, RSC Adv. **4**, 48848 (2014).

[40] N. Feng, W. B. Wen, X. C. Wang, and H. L. Bai, First-principles study on the interfacial magnetic and electronic properties of Fe_4N (001)/Si and Fe_4N(111)/graphene bilayers, Comput. Mater. Sci. **96**, 256 (2015).

[41] P. E. Blöchl, Projector augmented-wave method, Phys. Rev. B **50**, 17953 (1994).

[42] G. Kresse and J. Hafner, *Ab initio* molecular dynamics for liquid metals, Phys. Rev. B **47**, 558(R) (1993).

[43] G. Kresse and J. Furthmüller, Efficiency of ab-initio total energy calculations for metals and semiconductors using a plane-wave basis set, Comput. Mater. Sci. **6**, 15 (1996).

[44] G. Kresse and J. Furthmüller, Efficient iterative schemes for *ab initio* total-energy calculations using a plane-wave basis set, Phys. Rev. B **54**, 11169 (1996).

[45] J. P. Perdew, K. Burke, and M. Ernzerhof, Generalized Gradient Approximation Made Simple, Phys. Rev. Lett. **77**, 3865 (1996).

[46] B. Dieny and M. Chshiev, Perpendicular magnetic anisotropy at transition metal/oxide interfaces and applications, Rev. Mod. Phys. **89**, 025008 (2017).

[47] B. S. Yang, J. Zhang, L. N. Jiang, W. Z. Chen, P. Tang, X.-G. Zhang, Y. Yan, and X. F. Han, Strain induced enhancement of perpendicular magnetic anisotropy in Co/graphene and Co/BN heterostructures, Phys. Rev. B **95**, 174424 (2017).

[48] D.-S. Wang, R. Q. Wu, and A. J. Freeman, First-principles theory of surface magnetocrystalline anisotropy and the diatomic-pair model, Phys. Rev. B **47**, 14932 (1993).

[49] W. B. Mi, Z. B. Guo, X. P. Feng, and H. L. Bai, Reactively sputtered epitaxial γ-Fe_4N films: Surface morphology, microstructure, magnetic and electrical transport properties, Acta Mater. **61**, 6387 (2013).

[50] V. L. Moruzzi, P. M. Marcus, K. Schwarz, and P. Mohn, Ferromagnetic phases of bcc and fcc Fe, Co, and Ni, Phys. Rev. B **34**, 1784 (1986).

[51] K. Oda, T. Yoshio, and K. Oda, Preparation of Co-N films by rf-sputtering, J. Mater. Sci. **22**, 2729 (1987).

[52] M. Meinert, Exchange interactions and Curie temperatures of the tetrametal nitrides Cr_4N, Mn_4N, Fe_4N, Co_4N and Ni_4N, J. Phys. Condens. Matter **28**, 056006 (2016).

[53] P. Hemzalová, M. Friák, M. Šob, D. Ma, A. Udyansky, D. Raabe, and J. Neugebauer, *Ab initio* study of thermodynamic, electronic, magnetic, structural, and elastic properties of Ni_4N allotropes, Phys. Rev. B **88**, 174103 (2013).

[54] W. Tang, E. Sanville, and G. Henkelman, A grid-based Bader analysis algorithm without lattice bias, J. Phys. Condens. Matter **21**, 084204 (2009).

[55] E. Kisker, K. Schröder, W. Gudat, and M. Campagna, Spin-polarized angle-resolved photoemission study of the electronic structure of Fe (100) as a function of temperature, Phys. Rev. B **31**, 329 (1985).

[56] O. Wunnicke, N. Papanikolaou, R. Zeller, P. H. Dederichs, V. Drchal, and J. Kudrnovsky, Effects of resonant interface states on tunneling magnetoresistance, Phys. Rev. B **65**, 064425 (2002).

[57] C. Hu, J. Teng, G. H. Yu, W. G. Lu, and W. Ji, Conditions for quantized anisotropic magnetoresistance, Phys. Rev. B **91**, 045438 (2015).